Available online at www.sciencedirect.com

Manufacturing Letters

Manufacturing Letters 41 (2024) 742–752

52nd SME North American Manufacturing Research Conference (NAMRC 52, 2024)

An analytical model for estimating process parameters input in L-DED based on bead geometry

Kandice S. B. Ribeiro[a,*], Ana C. Reghini[b], Reginaldo T. Coelho[c]

[a] *Department of Mechanical and Materials Engineering, Faculty of Technology, University of Turku, Turku – 20520, Finland*
[b] *Department of Mechanical Engineering, São Carlos School of Engineering, University of São Paulo, São Carlos – 13566-690, Brazil*
[c] *Department of Production Engineering, São Carlos School of Engineering, University of São Paulo, São Carlos – 13566-690, Brazil*

Abstract

Additive manufacturing of metal alloys via laser Directed Energy Deposition (L-DED) has been gaining popularity due to its potential to repair and create new features/components, enabling new applications for built parts. The success of L-DED operations hinges on the precise control of printing parameters, including laser power, scanning speed, and powder feed rate. These parameters significantly influence heat distribution during printing, directly impacting the quality of the resulting parts. Thus, defining an efficient methodology to find a good correlation between these parameters for the printing process is crucial to boost part production, as it reduces the time-consuming trial-and-error parameter tuning process. In this context, our study introduces an analytical model that predicts printing parameters based on the deposited material volume along track lines. Deposition was carried in stainless steel 316L with different values for laser power (ranging from 500 to 750 W with 50 W increments), scanning speed (from 400 to 700 mm/min with 100 mm/min increments), and powder feed rate (6.4, 8.0 and 10.0 g/min). The experimental data verified the effectiveness of the proposed model, demonstrating its potential to standardize the first step of printing process and expedite the initial search for optimal printing parameters in L-DED. The model provided accurate initial estimates of laser power, with a maximum relative error of 12%, particularly for the optimum mass flow rate ($\dot{m}$) of 8.0 g/min. Beyond its benefits to the L-DED process, this analytical solution contributes to experimental practices by offering an efficient method for predicting material deposition volume during printing. Thus, our work underscores the significance of optimizing printing parameters to achieve high-quality parts and provides a valuable reference for future research and studies in the field of L-DED.

Keywords: Additive Manufacturing; Analytical model; Parameter prediction

1. Introduction

In modern industry, the seek for manufacturing processes able to produce parts with good quality parts amidst the shortest possible time and cost is constant [9, 27]. Regarding this scenario, Additive Manufacturing (AM) has been broadly explored [22]. Recent studies shows that metal AM, in particular, has been used in the manufacture of aerospace [15], automotive [21, 12] and medical [13] components. One of the most common reasons for the adoption of metal-AM technologies by industry are due to the possibility of producing featured parts of complex shapes that would be difficult, sometimes even impossible, to be manufactured by conventional methods alone, the production of lightweight and designed optimized structures [9, 27]. However, greater adoption of AM still depends on addressing some gaps in these technologies. Among the various challenges, insufficient repeatability, and consistency in the produced parts [11], and the lack of fundamental understanding of the impact of operational variables on part quality [30], are still to be solved to enable a greater adoption of AM technologies. In this regard, understanding the parameters of the process

---

[*] Corresponding author. Tel.: +358 50 .
E-mail address: ksbari@utu.fi (Kandice S. B. Ribeiro).

and their influences on the obtained results is essential for the strengthening of such technologies.

Among the seven standardized AM technologies, Directed Energy Deposition (DED) is defined by the American Society for Testing and Materials (ASTM) [1] as a additive manufacturing technology that adds material by the simultaneous delivery of feedstock and highly focused thermal energy to the workpiece, through a pre-define scanning strategy, layer by layer.

The DED process has many parameters, those which depend of the material and the machine used. Ahn [2] separates these parameters in four groups: laser, material & design, feeding, and motion & path. Out of these parameters, three – power (laser), scanning speed (motion & path) and powder mass flow rate (feeding) – have the greatest influence on the aspects of the resulting deposition (e.g. porosity, microstructure and residual stresses) [2]. Laser power determines the amount of energy that is used to melt substrate and powder, and it affects the geometry and properties of the deposition [28]. Insufficient power causes porosity and lack of fusion between substrate and deposited material, whilst excessive power may lead to distortions and residual stresses on the part produced [28]. The amount of incident energy on the substrate is also determined by the scanning speed, which indicates the time during which the laser is in contact with the material. Thus, a low scanning speed provokes a high dilution, and the opposite may cause lack of fusion and porosity [28].

Although the microstructure of the deposited part is influenced by the aspects of the utilized powder, it is mainly determined by the association of laser power and scanning speed [26]. For instance, a high scanning speed with a low laser power typically results in finer microstructures, while coarse microstructures can be obtained by a higher laser power and lower scanning speed [6, 32]. Li et al. [14] deposited the alloy Ni20 on a 316L stainless steel substrate to assess the influence of some parameters on layer height and bead width. Their influence on the height was equivalent to their influence on the amount of powder poured in the melting pool. In this way, the bead height increased with the increase of laser power and powder mass flow, and the decrease of scanning speed. The bead width often follows these patterns.

Sciammarella et al. [23] proposed a model of parameter optimization developed with the energetic analysis of the process in distinct experiments, in which mass flow rate ($\dot{m}$) and scanning speed (f) were varied, finding different values to the $\dot{m}/f$ ratio, which was found to be helpful on determining the quality of the deposition. The authors also concluded that the energetic aspect is important to the modeling of the process. The evaluation criteria for the deposited lines were: contact angle less than 110, Vickers hardness greater than 220 HVN, distribution of fine cellular substructure and low porosity levels. The track lines that have shown good results according to these criteria had a ratio $\dot{m}/f$ between 0.011 g/mm and 0.013 g/mm.

To validate the influence of this ratio, two tracks with values close to optimal and one with a lower value were chosen [23]. For each of these 5 sets of parameters, 3 blocks were deposited and their microstructure and hardness were analyzed. Both configurations chosen for having optimal $\dot{m}/f$ showed similar results. The two configurations with the value of this ratio lower than considered ideal had lower Vickers hardness and microsegregation, a consequence of remelting and resolidification caused by excess energy. For $\dot{m}/f = 0.011$, the porosity was higher than the previous ones, although the hardness was an intermediate value between the ideal configurations and those of higher $\dot{m}/f$. Thus, Sciammarella et al. [23] conclude that the ratio $\dot{m}/f$ can aid finding conditions for enhanced printing quality, and that the energetic aspect must be taken into account during the modeling of the process.

Boley et al. [5] also addressed the energetic aspect of DED. They applied ray tracing technology to model the laser absorption by different materials (Ag, Al, Au, Cu, SS and Ti) taking into account facets that previous models had not considered, such as the non-uniform absorption observed on low-porosity materials and the relationship between absorption and the ray angles and their polarization [5]. In their model, the powder particles were considered with spherical shape, and the laser hit perpendicularly in three distinct configurations: (i) flat surface, (ii) single sphere, and (iii) flat surface with two layers of powder particles, with the absorption in each layer being measured separately of each other and the substrate. For stainless steel, the flat surface presented an absorption of 0.34 of the laser rays, and the top layer absorbed 0.53.

The analytical model proposed by Elcheikh et al. [10] considered the correlation between the geometry of stainless steel 316L tracks on a low carbon substrate with laser power (180, 280 and 360 W), scanning speed (300, 600 and 900 mm/min) and powder mass flow rate (1.5, 3.0 and 4.5 g/min), on a factorial experiment. Two approaches were considered, (i) model relies on the bases that the powder distribution can govern the track geometry, and (ii) the track cross-section assumes the geometry of a disc regarding the tension forces acting at the surface. By fitting the experimental data into uniform, Gaussian and 2^{nd} degree polynomial distributions, the authors found out that the geometry was not influenced by the material distribution [10]. In addition, the proposed circular section approximated geometry was validated through the 27 tracks built. Although the proposed model is complex, having the shape of a single track approximated to a simple geometry, such as a circle, contributes to the bias that it is important to have simple models so they can be widely used and actually aid the definition of parameters in early stages of the printing.

Nenadl et al. [18] proposed a geometry prediction model also based on the three parameters used on the previously presented cases – laser power, scanning speed and powder mass flow – sustaining that these are the key parameters of the process, as they can be controlled and have a great influence on the result obtained. Other parameters (e.g. laser beam diameter and energy distribution, shielding and carrier gases) are needed to fully describe the process, but the variety of interactions and physical phenomena that occur make the complete process modeling a complex task. Nenadl et al. [18] analyzed parabolic, sinusoidal, elliptic and arc functions and obtained a model that predicts the geometry of one layer with the input of the three aforementioned parameters and the distance between adjacent beads. However, the formulated equations contain experimental constants, which are valid only to the experimental setup of that particular experiment.

The understanding and optimization of parameters is of great importance to the improvement of 3D printing processes [10]. Although there has been efforts to model and predict the best set of parameters for L-DED, a better understanding of the layer track as the basic geometry of a printed component, and a simple tool to aid the definition of parameters is still lacking towards a greener manufacturing.

In this regard, this paper presents the development of a novel analytical model for L-DED operations that is based on a simple approach that considers the bead geometric shape, having as the main output process parameters that can be used as a starting point for printing, and for other complex analytical solutions. It is noted that the establishment of a relationship between the parameters and the characteristics obtained in the deposited part is essential for a better understanding of L-DED and subsequent optimization of the results.

2. Analytical model

The proposed model attempts to estimate the total laser power (P_t) as a function of scanning speed (f) and powder mass flow ($\dot{m}$) required to produce a bead with a certain desired shape and dimensions. Important aspects from the cross section are the deposited bead area (A_b), dilution area (A_s) and heat affected zone (HAZ). The deposited track line can also be described in terms of bead width (w), height (h) and dilution depth (p). For optimal results, the bead cross section geometry must to be, according to cladding recommendations, similar to Fig. 1.

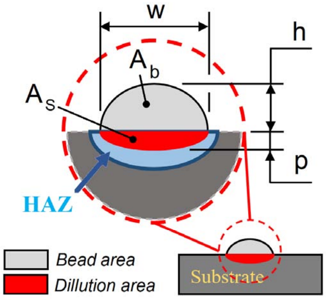

Figure 1. Theoretical bead geometry.

Besides the bead geometry, the thermophysical characteristics of the material (316L stainless steel) and the L-DED process characteristics are also considered in this model. Let the following assumptions be considered:

Assumption 1. The substrate in which the bead will be deposited has to be large enough to be considered a semi-infinite body;

Assumption 2. The processes of melting and solidification are fast enough for the convection to be ignored, at least within the range of temperatures in which no significant changes in bead shape occur [8].

The variables w, h and p (in Eq. 1-3), are to be obtained based on empiric knowledge about the deposition system used, which includes the laser and the printing nozzle with the present optical system. In this study, the following ratios were considered:

$$w = 0.8 \cdot d, \tag{1}$$

$$h = 0.45 \cdot w, \quad and \tag{2}$$

$$p = \frac{h}{3} \tag{3}$$

Where d is the spot diameter of the laser beam at the substrate.

The total power can be split into four groups, two related to the bead and two related to the substrate, as summarized in Figure 2.

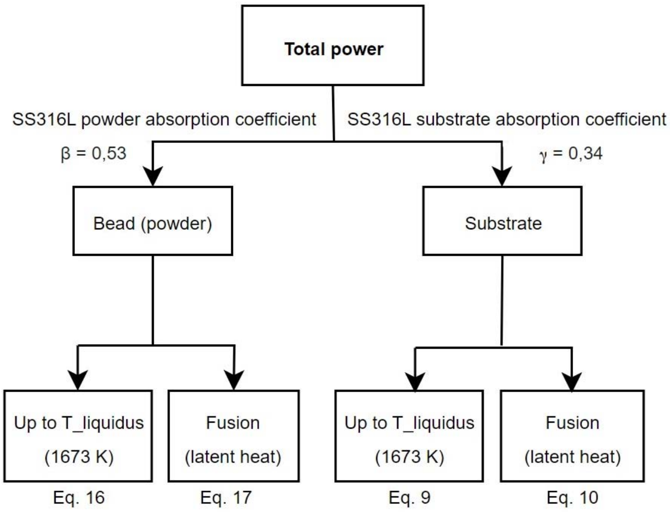

Figure 2. Schematics on the energy absorption in L-DED considering stainless steel 316L as powder and substrate material on the analytical model.

Initially, the laser beam has to melt the substrate in order to create a melt pool in which metal powder will be injected, mixed and solidified creating the DED bead, as schematically shown in Fig. 1. The power needed to melt the substrate, P_s, will be (Eq. 4):

$$P_s = P_{ss} + P_{sL} \tag{4}$$

Where P_{ss} is the power to heat the material to the fusion temperature and P_{sL} is the power associated with the latent heat of fusion, needed to keep it in liquid state. The power P_{ss} has to take into account that the laser beam is moving at speed f and must reach melting temperature at the depth p, enough to create the melt pool. Therefore, the substrate is a semi-infinite body with X and Y infinite axis and Z_+ only, as in Figure 3. In order to create a good melt pool for L-DED, Eq. 1 to Eq. 3 must be applied.

P_{ss} can be estimated based on heat transmission theory, well treated in Poirier and Geiger (2016) [20] and elaborated by

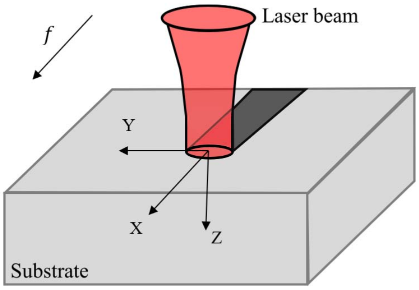

Figure 3. Melt pool referencing system adopted.

Carslaw and Jaeger [7]. Suppose that heat is supplied at the rate P per unit of time per unit area for $t > 0$ over the circle $x^2 + y^2 < r^2$, the temperature at the point $(0, 0, Z)$ is (Eq. 5):

$$\Theta = \frac{2\sqrt{\alpha t}}{K}\left[ierfc\left(\frac{Z}{2\cdot\sqrt{\alpha t}}\right) + ierfc\left(\frac{\sqrt{Z^2 + r^2}}{2\cdot\sqrt{\alpha t}}\right)\right] \tag{5}$$

Where α is the thermal diffusivity of the substrate, K is the thermal conductivity of the substrate, r is the radius of the heating source (laser) and $ierfc$ is the complementary-imaginary-error function, given by Eq. 6.

$$ierfc(x) = \frac{1}{\sqrt{\pi}} \cdot e^{-x^2} - x \cdot erfc(x) \tag{6}$$

Since the theory requires a time of exposure of the heating source over an area, the time in the DED process can be given by Eq. 7:

$$t = \frac{d}{f} \tag{7}$$

In addition, the bottom of the melt pool has to be increased until the material melting temperature, $\Delta\Theta_m = \Theta_m - \Theta_0$ in order to provide a good environment for the DED process. Being Θ_m and Θ_0 the temperatures of melting point and ambient, respectively. Therefore, working on Eq. 5 and simplifying it, Eq. 8 is obtained:

$$P_{ss} = \frac{K\Delta\Theta_m}{2\sqrt{\alpha t}}\left[\frac{e^{-A^2}}{\sqrt{\pi}} - A \cdot E(A) - \frac{e^{-B^2}}{\sqrt{\pi}} + B \cdot E(B)\right] \tag{8}$$

Where $A = 0.5Z(\alpha t)^{-1/2}$ and $B = 0.5\sqrt{(Z^2 + r^2)/(\alpha t)}$ in which $r = d/2$. E represents the complementary error function.

Using Eq. 8, the power to heat the substrate and create a melt pool, P_{ss}, is obtained as a function of the scanning speed, f, using t as in Eq. 7. Following that, P_{sL} – the power associated with the latent heat of fusion of the substrate – can be calculate as in Eq. 9:

$$P_{sL} = \dot{m}_s \cdot L_s \tag{9}$$

Where $\dot{m}_s$ is calculated as in Eq. 10:

$$\dot{m}_s = A_s \cdot f \cdot \rho \tag{10}$$

Where f is the scanning speed of the deposition head, ρ is the density of the substrate material and A_s is the area of the cross section of the dilution portion in the substrate (Fig. 1). Such area can be assumed as elliptical [18, 17, 19] and calculated, according to Fig. 1, as in Eq. 11:

$$A_s = \frac{\pi W p}{4} \tag{11}$$

Resuming Eq. 4 and introducing Eq. 10 and Eq. 11, the power required to create the melt pool on the substrate will be (Eq. 12):

$$P_s = P_{ss} + \frac{\pi W p}{4} \cdot \rho f L_s \tag{12}$$

However, when the laser beam interacts with the substrate material, part of it is reflected and does not contribute to the heating and melting of the substrate. The fraction actually heating varies depending on several conditions, such as angle of incidence, brightness of the surface, ambient temperature, etc. [25]. Using the absorptivity, γ, the power to create the melt pool becomes (Eq. 13). The absorption coefficient of the substrate was taken as 0.34, which was found in [5].

$$P_s = \frac{P_{ss}}{\gamma} + \frac{\pi W p}{4\gamma} \cdot \rho f L_s \tag{13}$$

In addition to that, the laser has to provide extra energy to melt the powder to create the bead. That power will have to heat the powder to its complete melting including the latent heat as well, P_b, which is given by Eq. 14:

$$P_b = P_{bs} + P_{bL} \tag{14}$$

Where P_{bs} is the power to heat the powder to the melting temperature and P_{bL} is the power associated with the latent heat of fusion, needed to keep the material in liquid state. The first part is given by Eq. 15, where m_p is the mass flux of powder and c_p denotes the specific heat of the powder, considered to be 500 $J/kg.K$.

$$P_{bs} = \dot{m}_p c_p \Delta\Theta_m \tag{15}$$

The latent power is calculated by Eq. 16, where L_b is the latent heat of fusion of the powder, taken to be the same used for the substrate, as they are both of the same material.

$$P_{bL} = \dot{m}_p \cdot L_b \tag{16}$$

Following the same idea applied for the substrate, the area of the bead (A_s in Fig. 1) is also calculated as half an ellipse. Thus, the power required to melt the powder and produce the bead is given by Eq. 17:

$$P_b = \frac{\pi W h}{4\beta} \cdot \rho f \cdot (c_{pb}\Delta\Theta_m + L_b) \tag{17}$$

Where β is the absorptivity of the powder material in sphere shape, as the case in the particular L-DED process hereby used

[5]. Therefore, the total energy for deposition is given by $P_s + P_b$, resulting in Eq. 18:

$$P_t = \frac{P_{ss}}{\gamma} + \frac{\pi W p}{4\gamma}\rho f L_s + \frac{\pi W h}{4\beta}\rho f\left(c_p \Delta\Theta + L_b\right) \tag{18}$$

After selecting an acceptable combination of P_t and f for deposition, based on the proposed model, the actual powder mass flow has to be estimated. Equation 10 gives the real mass after deposition, or the minimum acceptable flow, but the process has a mass efficiency, which depends on a long list of parameters, such as nozzle design, gas flows, laser power and scanning speed, just to mention some. Few publications deal with the subject and none was found addressing a method to asses such efficiency. At the moment, the first test, in which the model will be adjusted to fit existing data, such mass efficiency will be estimated for the nozzle employed in the current experimental setup.

3. Experimental setup

The experimental phase of this study was performed in a CNC L-DED machine model D800-Hybrid, manufactured by Indústrias ROMI, equipped with the AMBIT^{TM} laser-based system with the 2 mm laser spot size, manufactured by Hybrid Manufacturing Technologies.

The powder delivery system from this model is composed by a pressurized hopper that stores the powder under Argon gas controlled atmosphere, a rotatory disk and the conveying line. The hopper is set to keep the feedstock material at 60°C. At the outlet of the hopper, a stir is responsible for conducting and uniforming the powder to the rotatory disk. Thereupon, in this system, a tuning on the disk rotation adjusts the mass of powder delivered to the feed line.

To verify the powder deliver from the powder feeder, the mass flow rate out of the nozzle was measured by a precision digital scale Marte AC200 and plotted against the rotation speed (RPM) of the carrying disk. This test was conducted with constant deliver of Argon as for the nozzle, carrier and shield gases, set at 5, 6 and 12 L/min respectively, so the data would not be affected by the gases flow rate. As a result, stable operating zones were defined from 6 to 11 g/min.

To evaluate the influence of some process parameters to the bead geometry, single track lines were deposited in a full factorial design of experiments (DoE) of the main parameters governing the L-DED process: laser power (500, 550, 600, 650, 700 and 750 W), scanning speed (400, 500, 600 and 700 mm/min) and mass flow rate (6.4, 8.0 and 10.0 g/min), summing up to a total of 72 different conditions. A fixed conveying line of Argon gas was set at 6 L/min to carry the powder, a 5 L/min inner flow of gas to keep the pressure gradient and prevent powder and fumes to contaminate the optical lenses, and a local shielding atmosphere created by a 12 L/min flow rate at the outer exit of the deposition head. Table 1 shows these parameters.

Table 1. Printing parameters.

Parameters	Reference value
$\dot{m}$ (g/min)	6.4, 8.0, 10.0 g/min
P (W)	500, 550, 600, 650, 700, 750 W
f (mm/min)	400, 500, 600, 700 mm/min
Shield gas (L/min)	12 L/min
Carrier gas (L/min)	6 L/min
Nozzle gas (L/min)	5 L/min
Laser spot size (mm)	2.0 mm
Laser focal distance (mm)	10 mm

The material considered in this study was stainless steel 316L powder with particle size distribution ranging from 45 to 105 μm. Single bead lines 20 mm long were printed on a stainless steel 316L substrate (40 x 60 x 20 mm). The range of parameters were defined based on data available in previous publications with similar setup [24, 31, 29].

After printing test, the track lines were cut at 10 mm by wire-EDM, then hot mold, ground (120 to 1200 grit) and polished with diamond polishing paste 3 μm. All samples were submitted to an electrolytic etching with oxalic acid 10% w/v and 1.7 to 1.9 A during 15 s, to reveal the grain boundaries and easy the understanding on the different zones.

The bead cross-sections were evaluated with the aid of a 3D Laser Confocal microscope model LEXT OLS4100 manufactured by Olympus. The dimensions measured were later used as input to fit the proposed analytical model. Based on these inputs, the theoretical laser power required to originate that certain volume of deposition was calculated and compared with the experimental results.

Table 2 presents the thermal properties of stainless steel 316L applied on the analytical model previously presented. As the energetic aspect of the process has not been the focus of this study, the absorption coefficients calculated by Boley et al. [5] were used as reference values to the model.

Table 2. Thermal properties of stainless steel 316L [4, 3, 16]

Property	Symbol	Value
Liquidus temperature	Θ_m	1673 K
Density	ρ	8000 kg/m^3
Specific heat	c	500 $J/kg.K$
Latent heat of fusion	L	280000 J/kg
Thermal conductivity	K	22 $W/m.K$
Thermal diffusivity	α	5.144 . 10^{-6} m^2/s

4. Results and discussion

Fig. 4 presents the cross section of three beads deposited with $P = 600$ W and $f = 600$ mm/min at and different mass flow rates. In Fig. 4a, it is possible to see a bead with a flattened profile with $\dot{m} = 6.4$ g/min, whereas Fig. 4b shows an increase in the bead height when considering $\dot{m} = 8.0$ g/min. The increase of feedstock delivered to the melt pool promoted a rounder shape for the particular energy input. Thus, his increase in bead height is overall a reflection of the $\dot{m}$ increase. However, if the mass flow rate keeps on increasing, the system saturates and the rounded profile seen in Fig. 4b is lost and additional mass to the sides of the melt pool can be seen without dilution to the substrate, as shown in Fig. 4c.

Therefore, it is possible to state that the value of $\dot{m}$ influences the transverse shape of the beads, with the height of the bead increasing with the increase of $\dot{m}$, until the relation mass and energy input saturates, then there will be a more significant increase in the bead width. Another aspect to be considered is that the depth of the dilution to the substrate was similar in all three different mass flow rate, this being due to the fact that the energy input was the same in all three scenarios.

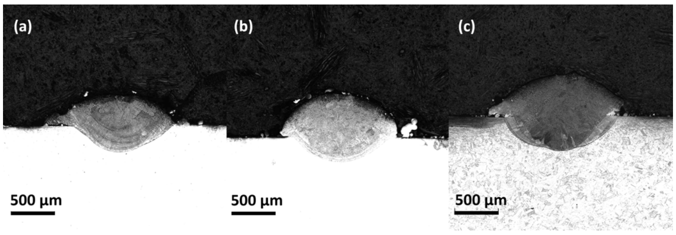

Figure 4. Cross section of the beads deposited with $P = 600\ W$ and $f = 600\ mm/min$ and different mass flow rates: (a) $\dot{m} = 6.4\ g/min$, (b) $\dot{m} = 8.0\ g/min$, and (c) $\dot{m} = 10.0\ g/min$.

The experimental data was used to validate and test the proposed analytical model and the results are thereby presented and analysed regarding each mass flow rate in the following subsections.

4.1. Model validation for $\dot{m} = 6.4\ g/min$

Fig. 5 presents the cross section of each one of the beads deposited with $\dot{m} = 6.4\ g/min$, in which w, h and p were used as input to estimate the laser power, so the relative error between each predicted laser power data point and its corresponding experimental value was calculated. Fig. 6 provides a visualization of both laser power values (experimental and predicted) and a trend line on the average predicted laser power for each scanning speed on the range. This way, it is possible to notice that the predicted laser power rise with the increase in scanning speed. This behavior is expected in order to keep the energy density level to melt the feedstock and substrate materials.

The linear trend equation obtained for $\dot{m} = 6.4\ g/min$ is given by Eq. 19, and the coefficient of determination R^2 (square of the correlation coefficient) found is indicated by Eq. 20. The low coefficient of determination indicates that the obtained values do not have a strong linear trend, with distant relationship between this coefficient and the accuracy of the model. As for accuracy, it can be observed that the lowest errors were obtained mostly in the beads deposited with the lowest values of P_{real} (between 500 e 650 W, except when $f = 700\ mm/min$). This indicates that the losses accounted by the model are consistent with what happens in the deposition process within this power range, i.e. for scanning speed between 400 mm/min and 600 mm/min. For $f = 700\ mm/min$, the obtained values for P_t were almost all higher than the power actually used, indicating an overestimation of the losses. This may be due to the fact that, with a higher scanning speed, the time of exposure of the material to the laser energy is shorter than in the previous cases, and this reduction in time changes the dynamics of the losses of the process.

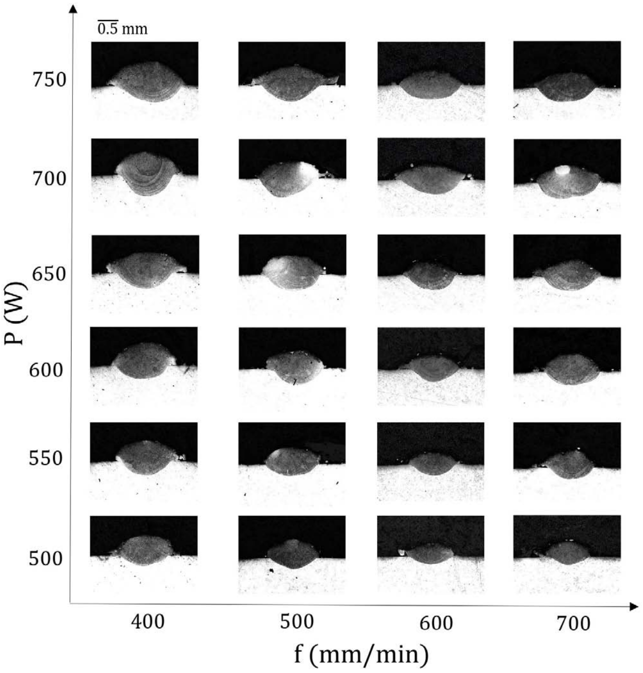

Figure 5. Cross section of the beads deposited with $\dot{m} = 6.4\ g/min$ for laser power $(500 - 750W)$ and scanning speed $(400 - 700mm/min)$.

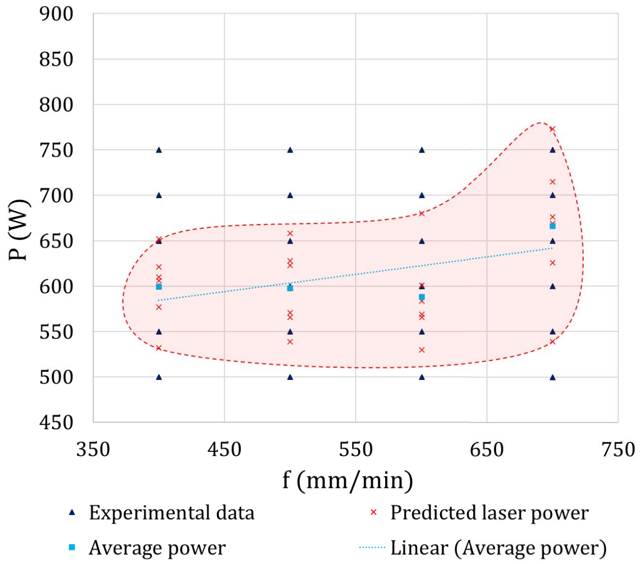

Figure 6. Comparison between experimental and predicted laser power for $\dot{m} = 6.4\ g/min$.

$$P = 0.1908f + 508 \tag{19}$$

$$R^2 = 0.4704 \tag{20}$$

4.2. Model validation for $\dot{m} = 8.0\ g/min$

Similarly to the previous presented set, Fig. 7 shows the cross section of each deposited bed with $\dot{m} = 8.0\ g/min$, whereas Fig. 8 presents the experimental and predicted data. Comparing the relative errors with the values obtained for $\dot{m} = 6.4\ g/min$, it has been noted that the magnitude of the errors for $\dot{m} = 8.0\ g/min$ is lower than those obtained in the previous case, indicating that the method used in the model estimates the losses that occur at 8.0 g/min better than at 6.4 g/min. The linear trend shows the average laser power from each scanning speed, with equation and coefficient of determination given by Eq. 21 and 22, respectively.

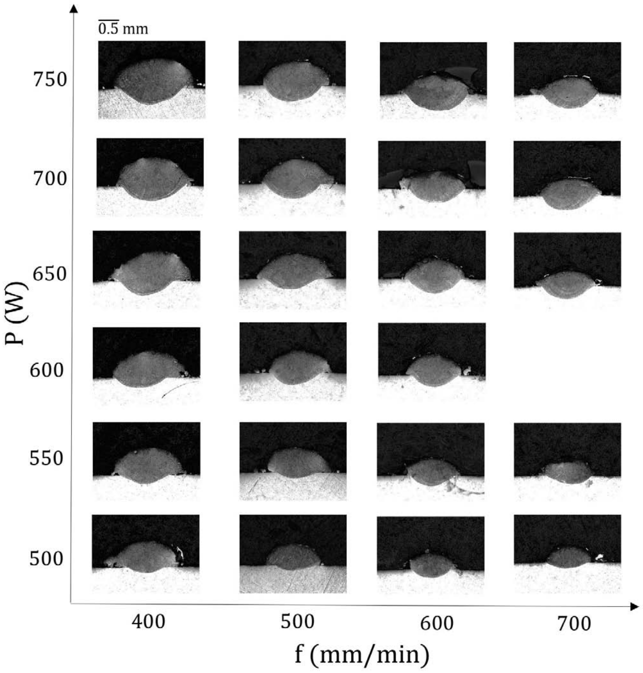

Figure 7. Cross section of the beads deposited with $\dot{m} = 8.0\ g/min$ for laser power $(500-750W)$ and scanning speed $(400-700mm/min)$.

$$P = 0.2023f + 511.72 \tag{21}$$

$$R^2 = 0.7814 \tag{22}$$

It can be seen that the region of occurrence of the predicted points is greater than for $\dot{m} = 6.4\ g/min$, which is expected considering that the obtained errors were lower. For $f = 600\ mm/min$ and $f = 700\ mm/min$, almost all predicted laser power values were higher than the real ones, also indicating an overestimation of the losses, but in a less accentuated way as noted for $\dot{m} = 6.4\ g/min$. Thus, the model offers a good approximation of laser power to be applied when $\dot{m} = 8.0\ g/min$.

4.3. Model validation for $\dot{m} = 10.0\ g/min$

Last but not least, Fig. 9 shows the cross sections of the remaining beads deposited with $\dot{m} = 10.0\ g/min$, and Fig. 10 presents the experimental data and the model prediction zone. The linear trend shows the average laser power from each scanning speed, with equation and coefficient of determination given by Eq. 23 and 24, respectively. All but two of the relative error values are positive, which leads to an overestimation of losses for the entire case of $\dot{m} = 10.0\ g/min$, which is visible in Fig. 10. This indicates that the losses considered in the model calculations have a certain mass flow rate limit for which can be considered credible. Thus, for $\dot{m} = 10.0\ g/min$, the losses were overestimated, with the mass being more effectively captured by the melt pool, resulting in a power higher than the power actually used in the depositions. Such occurrence might be related to the change in the characteristics of the melt pool when more mass is deposed into it, since it involves thermofluidic aspects that are not within the scope of this work.

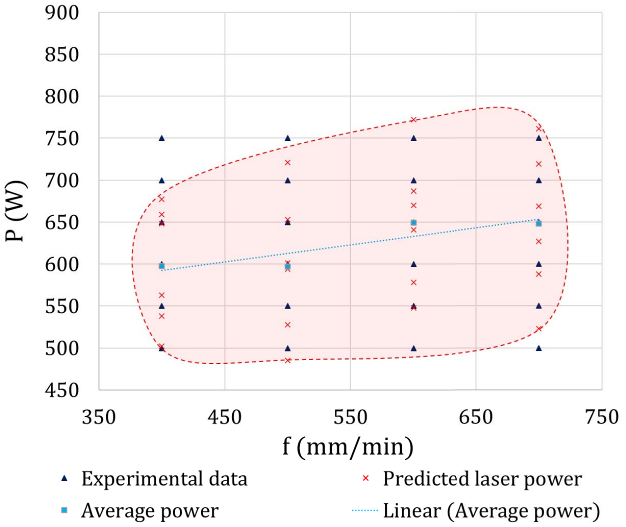

Figure 8. Comparison between experimental and predicted laser power for $\dot{m} = 8.0\ g/min$.

$$P = 0.1332f + 627.8 \tag{23}$$

$$R^2 = 0,9032 \tag{24}$$

4.4. Influence of different mass flow rates on the analytical model

In the three cases shown (Figures 6, 8 and 10), the trend line displayed a crescent behavior. The fitting equations obtained for $\dot{m} = 6.4\ g/min$ and $\dot{m} = 8.0\ g/min$ (equations 19 and 21) demonstrated great similarity, since both their angular coefficients (0.1908 and 0.2023) and linear coefficients (508 and 511.72) are close. This indicates that the laser power predicted by the proposed model, in both cases, are located approximately in the same range of values. However, this is not true when $\dot{m} = 10.0\ g/min$, as the equation differs significantly from the previous ones.

Figure 11 presents the relative errors obtained for the values of $\dot{m} = 6.4\ g/min$, $\dot{m} = 8.0\ g/min$ and $\dot{m} = 10.0\ g/min$ and the linear trend lines for each one of these sets. Again, it has

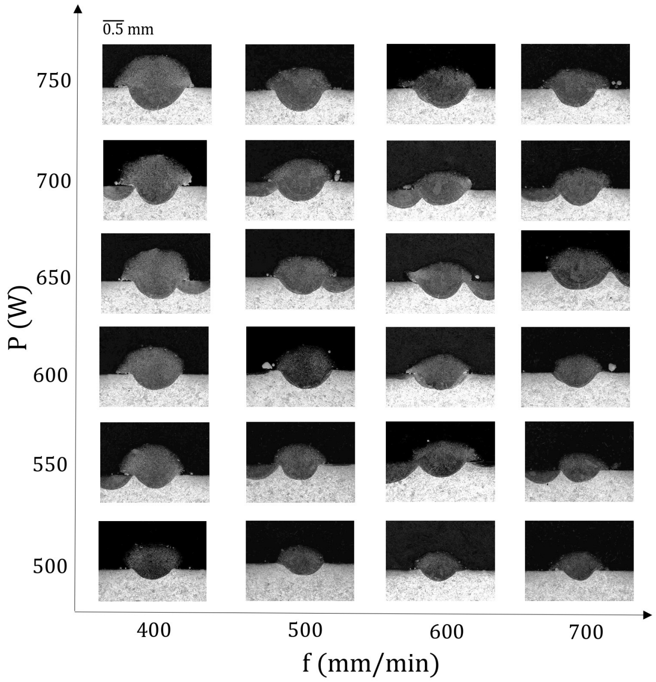

Figure 9. Cross section of the beads deposited with $\dot{m} = 10.0\ g/min$ for laser power $(500 - 750W)$ and scanning speed $(400 - 700mm/min)$.

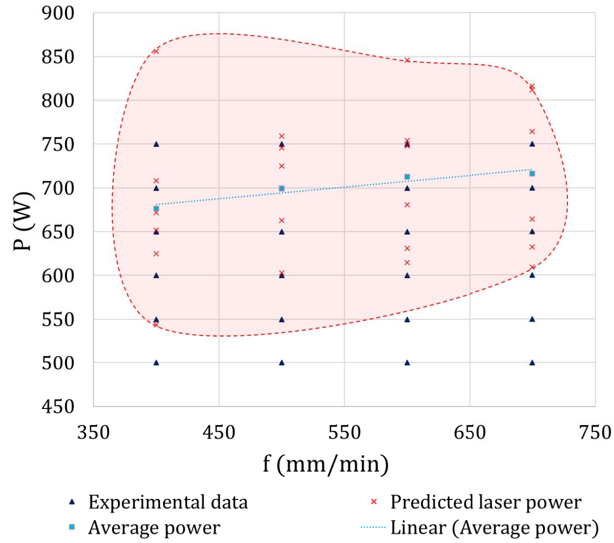

Figure 10. Comparison between experimental and predicted laser power data for $\dot{m} = 10.0\ g/min$.

been shown that the mass flow rate influences the accuracy of the model, which is well suitable for optimum range of mass delivered to the melt pool, i.e. $\dot{m} = 8.0\ g/min$ in this setup, as the goal of obtaining a good initial estimate for laser power, when given a scanning speed and considered bead geometry in ellipse shape.

To analyze as well the influence of the scanning speed on the relative error, it was made a variability plot considering both the laser power and the scanning speed, as presented on Figure 12.

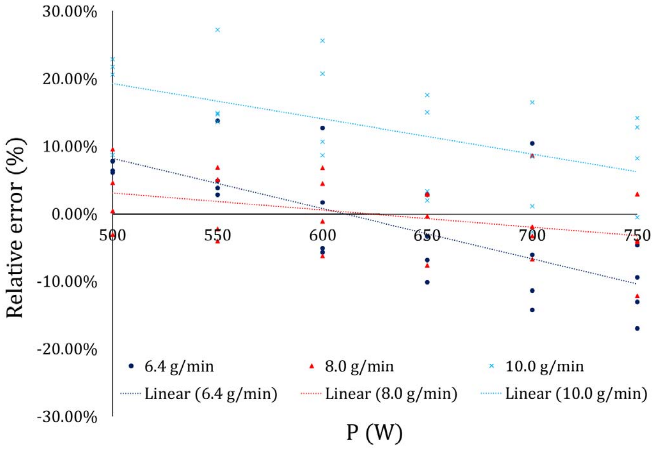

Figure 11. Relative error between experimental and predicted laser power data.

The lowest variance regarding the scanning speed is observed at $f = 700\ mm/min$, and it is also noted that, for this case, most of the relative errors are positive, contrary to what happens for other scanning speeds. However, it is seen that, for $f = 400\ mm/min$ and $f = 500\ mm/min$, most of the points are closer to zero. Concerning the laser power, the value with the lowest variance in terms of relative errors is $P = 650\ W$, with points fairly close to zero as well.

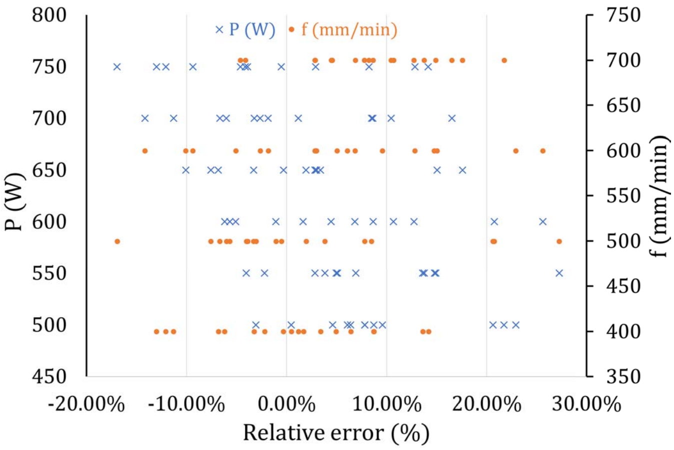

Figure 12. Variability of relative error considering the laser power and the scanning speed.

Notwithstanding, some of the deposited beads deviated the ideal shape considered for the model (represented by equations 1 to 3). Therefore, the lines closer to these proportions (based on the elliptical approximation showed in Fig. 1) were chosen to better specify the model's ability to predict the laser power to be used given the initial bead geometry and scanning speed. Some good examples of beads are presented in Fig. 13, in which all three were deposited with the hopper optimum delivery rate of $\dot{m} = 8\ g/min$. When considering the bead geometry presented in Fig. 13a, the relative error between the laser power predicted by the model and the experimental laser power was

2.20%. Likewise, for Fig. 13b and Fig. 13c, the relative error was 1.08%, and 1.86%, respectively.

Some of the higher relative errors presented before (Fig. 11) can be attributed to the deviation between the actual and estimated geometry of the beads. Features like a larger width, and height or excessive dilution were observed in some of the deposited beads can support the model's inaccuracy in such cases, as the model was based on a ideal ellipse geometry. Figure 14 presents some of these bad bead shapes: bead with excessive material on the sides (Fig 14a), in which the relative error of −16.94% can be due to the mass saturation or insufficient energy at the melt pool, and the mass excess that can increase the laser reflection – not explored in the model. On the other hand, Fig. 14b shows a typical bead with excessive dilution, and as deployed before in section 4.3, excessive mass rate delivery often changes the behavior of the melt pool, supporting the relative error of 14.17% obtained for this particular set with $\dot{m} = 10.0\ g/min$, $f = 400\ mm/min$ and $P = 750\ W$.

5. Conclusions

In this work, a novel analytical model was proposed and evaluated for different L-DED printing conditions. Altogether 72 single track beads in stainless steel 316L were deposited. The cross section of each one of the beads was analyzed in terms of bead height, bead width and dilution depth. Such values were used as experimental data to validate the proposed analytical model. Within these measurements, the scanning speed and mass flow rate, the model is able to predict the laser power required to perform each deposition when considering a bead shape geometry of ellipse. This way, it was possible to establish an analytical model fundamentally based on thermal aspects of the process, starting from two process parameters and the desired geometry of the bead, towards an initial estimation of the laser power required to perform single track beads with quality. Evaluating the results, it was observed that, at a given mass flow, the laser power predicted by the proposed model presented a crescent behavior with the increase of the scanning speed, as discussed in section 4.1. Also, the predicted laser power values have shown to be valuable inputs when optimizing the time consumed during the initial guess on the parameters, when considering the system's optimal material feed rate – $\dot{m} = 8.0\ g/min$ in this case study. For $\dot{m} = 6.4\ g/min$ and especially for $\dot{m} = 10.0\ g/min$, the accuracy of the model deviated more, as it tended to overestimate the energy losses in some cases. It is worth emphasizing that defining the parameters is a critical step when configuring the printing machine for various geometries. For optimal parameter definition, we need to evaluate four different geometries: (i) single beads, (ii) thin walls, (iii) single layers, and (iv) blocks. This process can be time-consuming and typically requires highly trained personnel. In its early development stages, our model also serves as a step towards making L-DED technologies more accessible and facilitating their broader adoption among end users. It can help bridge the gap and streamline the setup process for this innovative technology.

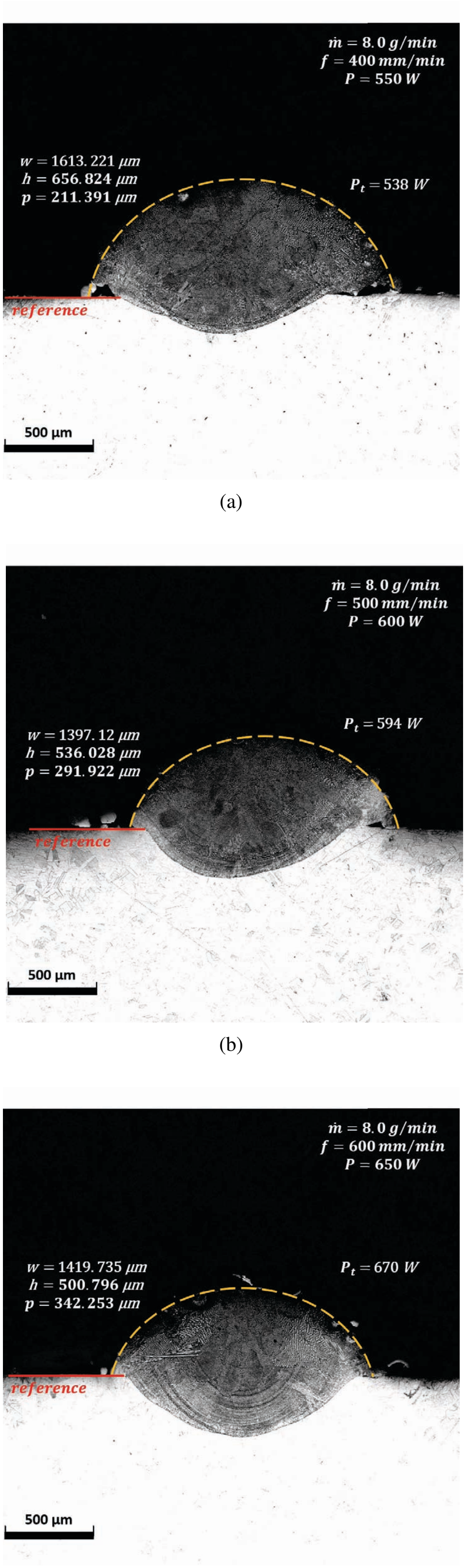

(a)

(b)

(c)

Figure 13. Typical bead cross sections with low geometry deviation and low relative errors of (a) 2.20%, (b) 1.08%, and (c) 1.86%.

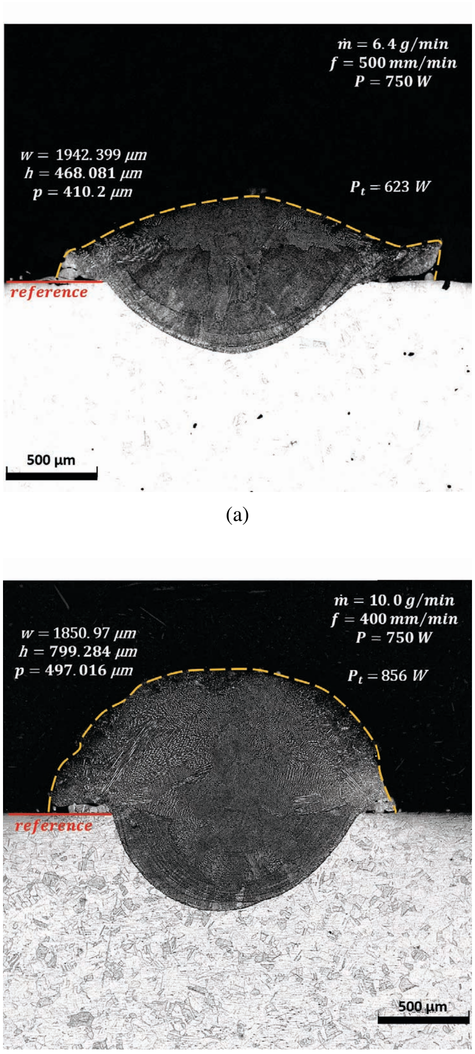

(a)

(b)

Figure 14. Typical bead cross sections with high geometry deviation and high relative errors of (a) −16.94% and (b) 14.17%.

Therefore, the limitations of the proposed model include, as said, the overestimation of energy losses in some cases, resulting in a relative low statistical performance. To improve this, further work needs to be done regarding the laser absorption and reflection by the material (powder and substrate). To improve the model and study its application on more realistic cases, more depositions in different geometries (walls, layers and blocks), as aforementioned, would also be valuable.

Acknowledgments

This work was fully supported by grants #2016/11309 – 0, #2019/00343 – 1 and #2021/10167 – 6, São Paulo Research Foundation (FAPESP).

Conflict of interest/Competing interests

The authors declare that they have no conflict of interest.

References

[1] 52910:2018(E), I., 2018. Additive manufacturing – Design – Requirements, guidelines and recommendations. 1st ed., ISO/ASTM International, 100 Barr Harbor Drive, PO Box C700, West Conshohocken, PA 19428-2959. United States.

[2] Ahn, D.G., 2021. Directed energy deposition (DED) process: State of the art 8, 703–742. URL: https://doi.org/10.1007/s40684-020-00302-7, doi:10.1007/s40684-020-00302-7.

[3] Ansari, P., Rehman, A., Pitir, F., Veziroglu, S., Mishra, Y., Aktas, O., Salamci, M., 2021. Selective laser melting of 316l austenitic stainless steel: Detailed process understanding using multiphysics simulation and experimentation doi:10.3390/met11071076.

[4] ASM Aerospace Specification Metals, Inc., 2022. Aisi type 316l stainless steel, annealed bar. URL: https://asm.matweb.com/search/SpecificMaterial.asp?bassnum=mq316q. acessado em: 30 de junho de 2022.

[5] Boley, C., Khairallah, S., Rubenchik, A., 2015. Calculation of laser absorption by metal powders in additive manufacturing. Applied Optics 54, 2477. doi:10.1364/AO.54.002477.

[6] Bontha, S., Klingbeil, N.W., Kobryn, P.A., Fraser, H.L., 2006. Thermal process maps for predicting solidification microstructure in laser fabrication of thin-wall structures 178, 135–142. URL: https://www.sciencedirect.com/science/article/pii/S0924013606002949, doi:10.1016/j.jmatprotec.2006.03.155.

[7] Carslaw, H., Jaeger, J., 1959. Conduction of Heat in Solids. Oxford University Press.

[8] Dass, A., Moridi, A., 2019. State of the art in directed energy deposition: From additive manufacturing to materials design 9, 418. doi:10.3390/coatings9070418.

[9] DebRoy, T., Wei, H.L., Zuback, J.S., Mukherjee, T., Elmer, J.W., Milewski, J.O., Beese, A.M., Wilson-Heid, A., De, A., Zhang, W., 2018. Additive manufacturing of metallic components – process, structure and properties. Progress in Materials Science 92, 112–224. URL: http://www.sciencedirect.com/science/article/pii/S0079642517301172, doi:10.1016/j.pmatsci.2017.10.001.

[10] El Cheikh, H., Courant, B., Branchu, S., Hascoët, J.Y., Guillén, R., 2012. Analysis and prediction of single laser tracks geometrical characteristics in coaxial laser cladding process. Optics and Lasers in Engineering 50, 413–422. URL: https://www.sciencedirect.com/science/article/pii/S0143816611003034, doi:https://doi.org/10.1016/j.optlaseng.2011.10.014.

[11] Huang, Y., Leu, M., Mazumder, J., Donmez, A., 2015. Additive manufacturing: Current state, future potential, gaps & needs, and recommendations URL: https://tsapps.nist.gov/publication/get_pdf.cfm?pub_id=916019.

[12] Jankovics, D., Barari, A., 2019. Customization of Automotive Structural Components using Additive Manufacturing and Topology Optimization. IFAC-PapersOnLine 52, 212–217. URL: https://www.sciencedirect.com/science/article/pii/S2405896319309218, doi:10.1016/j.ifacol.2019.10.066.

[13] Javaid, M., Haleem, A., 2018. Additive manufacturing applications in medical cases: A literature based review. Alexandria Journal of Medicine 54, 411–422. URL: https://www.sciencedirect.com/science/article/pii/S2090506817302282, doi:10.1016/j.ajme.2017.09.003.

[14] Li, Y., Yang, H., Lin, X., Huang, W., Li, J., Zhou, Y., 2003. The influences of processing parameters on forming characterizations during laser rapid forming 360, 18–25. URL: https://www.sciencedirect.com/science/article/pii/S0921509303004350, doi:10.1016/S0921-5093(03)00435-0.

[15] Liu, R., Wang, Z., Sparks, T., Liou, F., Newkirk, J., 2017. Aerospace applications of laser additive manufacturing. Elsevier Ltd. URL: http://dx.doi.org/10.1016/B978-0-08-100433-3.00013-0, doi:10.1016/B978-0-08-100433-3.00013-0.

[16] Mills, K., 2002. Recommended Values of Thermophysical Properties for Selected Commercial Alloys. Woodhead Publishing.

[17] Nenadl, O., Kuipers, W., Koelewijn, N., Ocel´k, V., De Hosson, J.T.M., 2016. A versatile model for the prediction of complex geometry in 3D direct laser deposition. Surface and Coatings Technology 307, 292–300. URL: https://www.sciencedirect.com/science/article/pii/S0257897216308544, doi:10.1016/j.surfcoat.2016.08.090.

[18] Nenadl, O., Ocel´k, V., Palavra, A., Hosson, J., 2014. The Prediction of Coating Geometry from Main Processing Parameters in Laser Cladding. Physics Procedia 56, 220–227. URL: https://www.sciencedirect.com/science/article/pii/S1875389214003113, doi:https://doi.org/10.1016/j.phpro.2014.08.166.

[19] Ocel´k, V., Nenadl, O., Palavra, A., De Hosson, J.T.M., 2014. On the geometry of coating layers formed by overlap. Surface and Coatings Technology 242, 54–61. URL: https://www.sciencedirect.com/science/article/pii/S0257897214000346, doi:10.1016/j.surfcoat.2014.01.018.

[20] Poirier, D.R., Geiger, G.H., 2016. Conduction of Heat in Solids. Springer International Publishing, Cham. pp. 281–327. URL: https://doi.o10.1007/978-3-319-48090-9_9, doi:10.1007/978-3-319-48090-9_9.

[21] Sarvankar, S.G., Yewale, S.N., 2019. Additive Manufacturing in Automobile Industry. International Journal of Research in Aeronautical and Mechanical Engineering 7, 01–10. URL: https://www.academia.edu/38718198/Additive_Manufacturing_in_Automobile_Industry.

[22] Schmidt, M., Merklein, M., Bourell, D., Dimitrov, D., Hausotte, T., Wegener, K., Overmeyer, L., Vollertsen, F., Levy, G.N., 2017. Laser based additive manufacturing in industry and academia. CIRP Annals 66, 561–583. URL: http://www.sciencedirect.com/science/article/pii/S0007850617301506, doi:10.1016/j.cirp.2017.05.011.

[23] Sciammarella, F.M., Salehi Najafabadi, B., 2018a. Processing Parameter DOE for 316L Using Directed Energy Deposition. Journal of Manufacturing and Materials Processing 2. URL: https://www.mdpi.com/2504-4494/2/3/61, doi:10.3390/jmmp2030061. number: 3 Publisher: Multidisciplinary Digital Publishing Institute.

[24] Sciammarella, F.M., Salehi Najafabadi, B., 2018b. Processing parameter doe for 316l using directed energy deposition. Journal of Manufacturing and Materials Processing 2. URL: https://www.mdpi.com/2504-4494/2/3/61, doi:10.3390/jmmp2030061.

[25] Sears, J., 2007. Measuring laser absorption coefficient during laser additive manufacturing of 316l stainless steel and ti-6v-4al alloys, p. 401. doi:10.2351/1.5061066.

[26] Shamsaei, N., Yadollahi, A., Bian, L., Thompson, S.M., 2015. An overview of Direct Laser Deposition for additive manufacturing; Part II: Mechanical behavior, process parameter optimization and control. Additive Manufacturing 8, 12–35. URL: https://www.sciencedirect.com/science/article/pii/S2214860415000329, doi:10.1016/j.addma.2015.07.002.

[27] Strong, D., Kay, M., Conner, B., Wakefield, T., Manogharan, G., 2018. Hybrid manufacturing – integrating traditional manufacturers with additive manufacturing (am) supply chain. Additive Manufacturing 21, 159–173. URL: http://www.sciencedirect.com/science/article/pii/S2214860417305444, doi:10.1016/j.addma.2018.03.010.

[28] Sun, Z., 2019. Computational fluid dynamics modelling of powder-based laser additive manufacturing processes.

[29] Tan, Z.E., Pang, J.H.L., Kaminski, J., Pepin, H., 2019. Characterisation of porosity, density, and microstructure of directed energy deposited stainless steel aisi 316l. Additive Manufacturing 25, 286–296. URL: http://www.sciencedirect.com/science/article/pii/S2214860417304037, doi:10.1016/j.addma.2018.11.014.

[30] Tofail, S.A., Koumoulos, E.P., Bandyopadhyay, A., Bose, S., O'Donoghue, L., Charitidis, C., 2018. Additive manufacturing: scientific and technological challenges, market uptake and opportunities. Materials Today 21, 22–37. URL: https://www.sciencedirect.com/science/article/pii/S1369702117301773, doi:https://doi.org/10.1016/j.mattod.2017.07.001.

[31] Weng, F., Gao, S., Jiang, J., Wang, J., Guo, P., 2019. A novel strategy to fabricate thin 316l stainless steel rods by continuous directed energy deposition in z direction. Additive Manufacturing 27, 474–481. URL: http://www.sciencedirect.com/science/article/pii/S2214860418309175, doi:10.1016/j.addma.2019.03.024.

[32] Zheng, B., Zhou, Y., Smugeresky, J., Schoenung, J., Lavernia, E., 2008. Thermal behavior and microstructural evolution during laser deposition with laser-engineered net shaping: Part i. numerical calculations 39, 2228–2236. URL: https://doi.org/10.1007/s11661-008-9557-7, doi:10.1007/s11661-008-9557-7.